Dual Stator Winding Induction Machine Drive

Alfredo R. Muñoz, *Member, IEEE,* and Thomas A. Lipo, *Fellow, IEEE*

***Abstract*—A new dual stator winding induction machine drive is described in this paper. The proposed induction machine consists of a standard squirrel-cage rotor and a stator with two separate windings wound for a dissimilar number of poles. Each stator winding is fed from an independent variable-frequency variable-voltage inverter. The proposed drive offers such advantages as speed sensorless operation, better reliability, and more flexibility to manipulate the resultant torque–speed curve of the motor. In the proposed drive, zero-speed operation is achieved by independently controlling the two sets of stator currents, hence, maintaining a minimum electrical frequency independent of the mechanical speed. This feature is especially important to minimize the negative impact of the stator resistance influence at low-speed operation and it greatly simplifies the implementation of speed sensorless control schemes. The drive is well suited for either constant volts per hertz or field-oriented (FO) operation. Circulating harmonic currents, common to most dual stator machines, are eliminated by the dissimilar pole number in each stator winding.**

***Index Terms*—Dual stator, field orientation, induction machine, low speed, sensorless, volts per hertz.**

I. Introduction

BROADLY speaking, from the point of view of the stator winding, dual stator machines can be categorized as "*split-wound*" and "*self-cascaded*."

The *split-wound* machine was introduced in the 1920s as a means of increasing the total power capability of large synchronous generators [1]. Since then, they have been used in many other applications ranging from synchronous machines with ac and dc outputs [2], as part of uninterrupted power supplies (UPSs) [3] and as current-source inverters [4] to large pumps, compressors, and rolling mills. *Split-wound* machines made it possible to extend the power range of solid-state-based drives beyond the power capability of a single inverter and, more recently, new multilevel topologies have been introduced as well [5]. Additionally, due to the inherent redundancy, it is claimed that the system exhibits a better reliability [6]–[8]. In a *split-wound* machine, the stator winding consists of two similar but separate three-phase windings wound for the same number of poles. Both stators are fed with the same frequency and the rotor is a standard squirrel cage. The two stator windings are mutually coupled and small unbalances in the supplied voltages generate circulating currents. Furthermore, because of the low impedance to harmonic currents there is a high level of circulating currents when a nonsinusoidal voltage source supply is used [9], adding losses and demanding larger semiconductor device ratings.

The *self-cascaded* machine, also known as the *brushless doubly-fed machine* (BDFM), was first successfully introduced by Hunt in 1907 [10]. In order to incorporate the effects of a cascade connection, the BDFM requires a special rotor structure formed by several "nested" loops [11]. This results in a cumbersome "semi-cage"-like structure that does not lend itself for diecasting. Additionally, achieving the necessary insulation between rotor bars and stack remains a major technical challenge [12], [13]. This increases the cost and it constitutes one of the main drawbacks of the machine. In the past, BDFMs found some application in systems requiring low speed and where robustness and reliability were essential assets [11]. More recently, BDFMs have attracted renewed interest for narrow speed range applications [14], [15]. The speed is controlled by the secondary winding which only handles the slip power. For applications requiring a full speed range, the converter must be rated at full power and the advantage is lost. In addition, because of the cascade connection, the efficiency is inherently low and this system is not widely used.

The dual stator winding induction machine (DSIM) drive proposed here differs from other types of dual stator machines in that the two stator windings are wound for a dissimilar number of poles *and* the rotor is a standard diecast squirrel cage, the total kilovoltampere inverter rating is similar to that of a single stator machine, and it provides torque/speed control over a wide range. The drive offers such advantages as speed sensorless operation, better reliability, and full utilization of the stator windings at all times to produce useful torque. Since there is no winding reconnection of any sort the system can provide a fast dynamic response. Circulating harmonic currents due to mutual leakage coupling between the stator windings is eliminated by using a symmetric winding.

II. Dual Stator Winding IM Drive

The proposed induction machine consists of a standard diecast squirrel-cage rotor and a stator with two separate windings wound for a dissimilar number of poles (e.g., 2/6 or 4/12). Any combination of dissimilar pole numbers could be used, however to better utilize the magnetic material, avoid localized saturation, and additional stator losses, it is found that the most advantageous configuration should have a pole ratio 1 : 3. Each stator winding is fed from an independent variable-frequency variable-voltage inverter, sharing a common dc-bus. Fig. 1 shows the main components of the proposed DSIM drive.

To avoid deep saturation, the peak magnetic loading produced by the combined effect of the two stator MMFs must be similar

Paper IPCSD 00–020, presented at the 1998 Industry Applications Society Annual Meeting, St. Louis, MO, October 12–16, and approved for publication in the IEEE TRANSACTIONS ON INDUSTRY APPLICATIONS by the Industrial Drives Committee of the IEEE Industry Applications Society. Manuscript submitted for review May 1, 1998 and released for publication March 30, 2000.

A. R. Muñoz is with the Scientific Research Laboratory, Ford Motor Company, Dearborn, MI 48124-2053 USA (e-mail: amunoz6@ford.com).

T. A. Lipo is with the Department of Electrical and Computer Engineering, University of Wisconsin , Madison, WI 53706-1691 USA (e-mail: lipo@engr.wisc.edu).

Publisher Item Identifier S 0093-9994(00)07624-6.

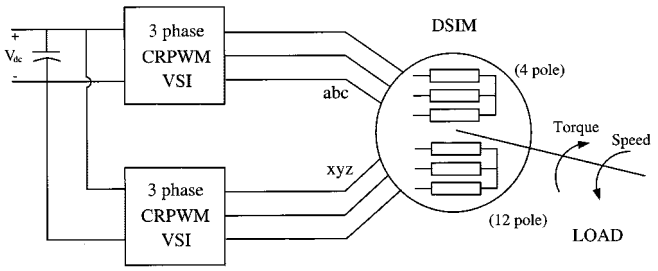

Fig. 1. Dual stator winding induction machine drive (DSIM).

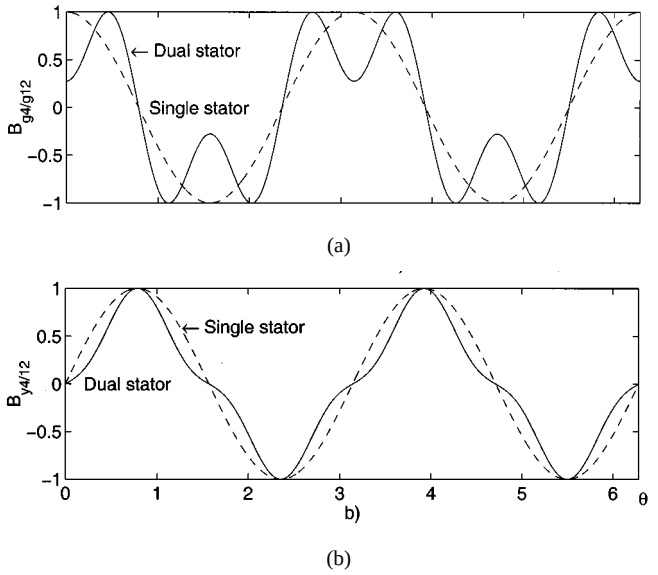

(a)

(b)

Fig. 2. Normalized flux density distributions for the DSIM. (a) Air gap. (b) Stator yoke.

to that of an equivalent single stator winding design. To maintain the saturation level in the stator teeth the peak air-gap flux density must be maintained. At the same time, to maintain the loading of the stator yoke, the peak flux density per pole must be identical in both the dual stator and single stator designs. Neglecting space harmonics, this is accomplished by choosing [16]

$$B_{g4} = 0.819 B_o$$
$$B_{g12} = 0.543 B_o \tag{1}$$

where B_o, B_{g4}, and B_{g12} are the peak air-gap flux densities produced by an equivalent single stator, the four-pole, and the 12-pole stator windings, respectively. This yields the spatial flux-density distributions of Fig. 2. The measured air-gap flux density for the prototype machine, under locked-rotor condition, is presented in Fig. 3; also included in this figure are the terminal currents of both windings. It is verified that the peak amplitudes of both waveforms are 1 pu. It is also important to point out that, although the peak magnetic field in the stator is the same in both cases, the DSIM is less saturated with the exception of the point at which the peak occurs. Thus, it is expected that the iron losses in the yoke of the DSIM should be reduced. The rotor of the DSIM is a standard squirrel cage, which guarantees that both stator current distributions will simultaneously couple with the rotor flux to produce the desired torque.

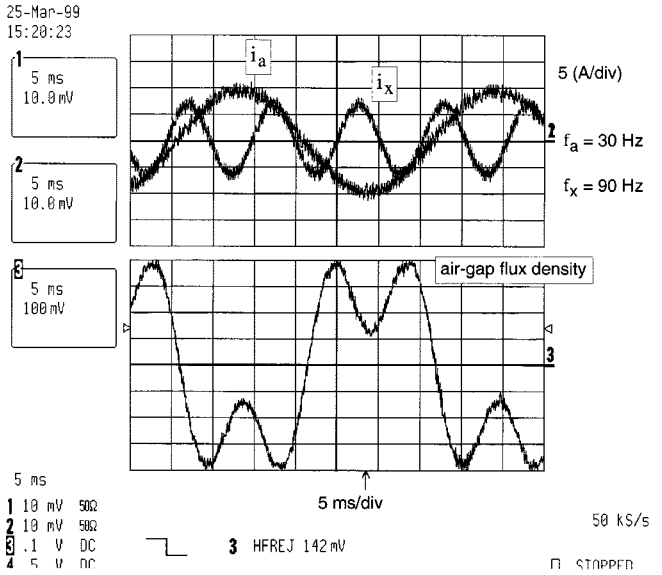

Fig. 3. Measured flux density distribution for the DSIM (top: stator currents; bottom: air gap flux density).

Because of the decoupling effect produced by windings with dissimilar pole number, the DSIM behaves as two independent induction machines mechanically coupled through the shaft. Therefore, for a given operating condition, the stator frequency is determined by the combination of the rotor speed, slip frequency, and the added variable of a second torque component. This feature is advantageous to implement simpler speed sensorless schemes.

The stator frequency of the low-pole number winding can be boosted by applying a controlled amount of torque with the high-pole number winding, hence limiting the minimum electrical frequency in the low-pole number winding to a predetermined value. This reduces the impact of the stator resistance voltage drop in the stator voltage measurement and simplifies the estimation of the rotor flux vector. This is especially important at zero speed, where the normal induction machine becomes unobservable. In the DSIM, zero-speed operation does not translate into zero excitation frequency, making the system observable at all speeds. Two distinct operating modes are considered: *synchronous* operation, where the two frequencies fed to the machine are in the same ratio as the pole number, and *asynchronous* operation, where the frequency in the low-pole number winding is held constant at a minimum value. This is shown in Fig. 4. A detailed discussion of the control scheme is presented in Section IV.

III. Machine Model

Analyses of induction motors are routinely carried out by replacing the squirrel cage by an equivalent sinusoidally distributed winding. This is done under the assumption that high-order space harmonics can be neglected. Given the particular characteristics of the machine considered in this study, having two simultaneous MMFs distributions that move in space with respect to each other and to the rotor bars, it is critical to clarify the interaction between the instantaneous rotor bar

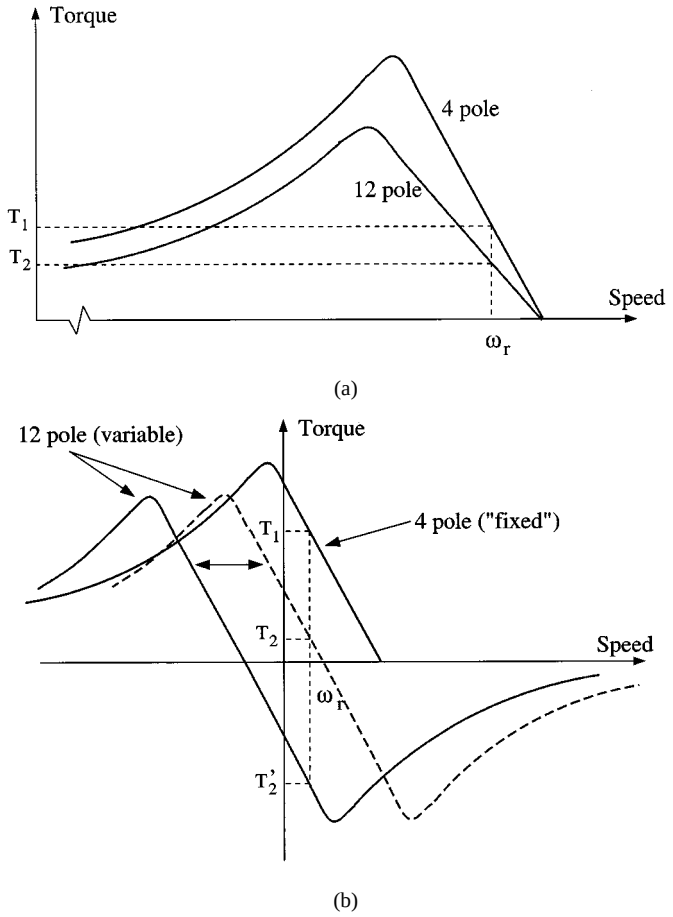

Fig. 4. General control strategy. (a) Synchronuos operation. (b) Asynchronous operation.

currents and the stator MMFs, as well as the possible interaction between the two stator windings. For this purpose, a detailed, yet simple, dynamic model of the machine was developed. Coupled magnetic circuit theory and complex space-vector notation is used throughout the derivation. This technique was chosen because of its generality and the great deal of simplification that is achieved. The following general assumptions are made:

- negligible saturation;
- uniform air gap;
- stator windings sinusoidally distributed;
- no electrical interconnection between stators;
- negligible inter-bar current.

It is also assumed that the two stator windings are wound for two and P poles, respectively, and that one stator is displaced with respect to the other by a fixed but arbitrary angle ξ. The low-pole number winding is referred to as abc and the high-pole number winding as xyz. The rotor is a standard squirrel cage. The windings and rotor of the DSIM are schematically shown in Fig. 5.

A. Stator Flux

If the stator windings are sinusoidally distributed in space but wound for a dissimilar number of poles, there is no mutual coupling between them [17], [18]. Real distributed windings, on the other hand, will produce space harmonics. If the pole ratio

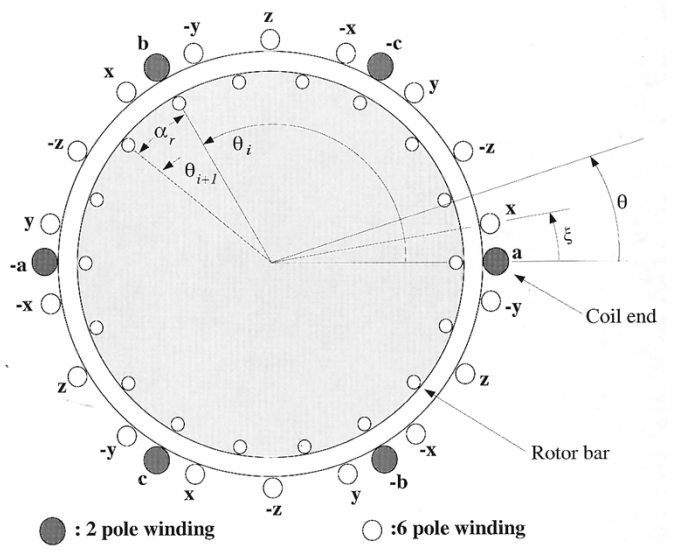

Fig. 5. DSIM windings distribution.

between the windings is $1:3$, the only common harmonics are those of triple order, but, in the absence of a neutral connection, triple harmonics are eliminated. Thus, even if real windings are considered, there will be no mutual coupling due to space harmonics. However, since both windings share common slots and are in close proximity, there is a common leakage flux linking them. This gives rise to the so-called mutual leakage coupling [3], [19].

The total flux linked by the stator windings and due only to the stator currents $\boldsymbol{i}_{sabc}$ and $\boldsymbol{i}_{sxyz}$ can be written, in matrix form, as

$$\begin{bmatrix} \boldsymbol{\Lambda}_{ssabc} \\ \boldsymbol{\Lambda}_{ssxyz} \end{bmatrix} = \begin{bmatrix} \boldsymbol{L}_{s1} & \boldsymbol{L}_{s12} \\ \boldsymbol{L}_{s21} & \boldsymbol{L}_{s2} \end{bmatrix} \begin{bmatrix} \boldsymbol{i}_{sabc} \\ \boldsymbol{i}_{sxyz} \end{bmatrix} \tag{2}$$

where

$$\begin{bmatrix} \boldsymbol{\Lambda}_{ssabc} \\ \boldsymbol{\Lambda}_{ssxyz} \end{bmatrix} = \begin{bmatrix} \lambda_{ass} \\ \lambda_{bss} \\ \lambda_{css} \\ \lambda_{xss} \\ \lambda_{yss} \\ \lambda_{zss} \end{bmatrix} \quad \begin{bmatrix} \boldsymbol{i}_{sabc} \\ \boldsymbol{i}_{sxyz} \end{bmatrix} = \begin{bmatrix} i_{as} \\ i_{bs} \\ i_{cs} \\ i_{xs} \\ i_{ys} \\ i_{zs} \end{bmatrix}. \tag{3}$$

$\boldsymbol{L}_{s1}$ and $\boldsymbol{L}_{s2}$ represent the self-inductance matrices of the abc and xyz windings respectively. They are of the form

$$\boldsymbol{L}_{si} = \begin{bmatrix} L_{lsi} + L_{msi} & -\frac{L_{msi}}{2} & -\frac{L_{msi}}{2} \\ -\frac{L_{msi}}{2} & L_{lsi} + L_{msi} & -\frac{L_{msi}}{2} \\ -\frac{L_{msi}}{2} & -\frac{L_{msi}}{2} & L_{lsi} + L_{msi} \end{bmatrix}. \tag{4}$$

The winding self-magnetizing inductance L_{msi} is known to be [17]

$$L_{msi} = \frac{\pi \mu_o l r}{g} \left(\frac{N_{si}}{P} \right)^2 \tag{5}$$

where N_{si} is the effective number of turns of each sinusoidally distributed winding, and the total per-phase magnetizing induc-

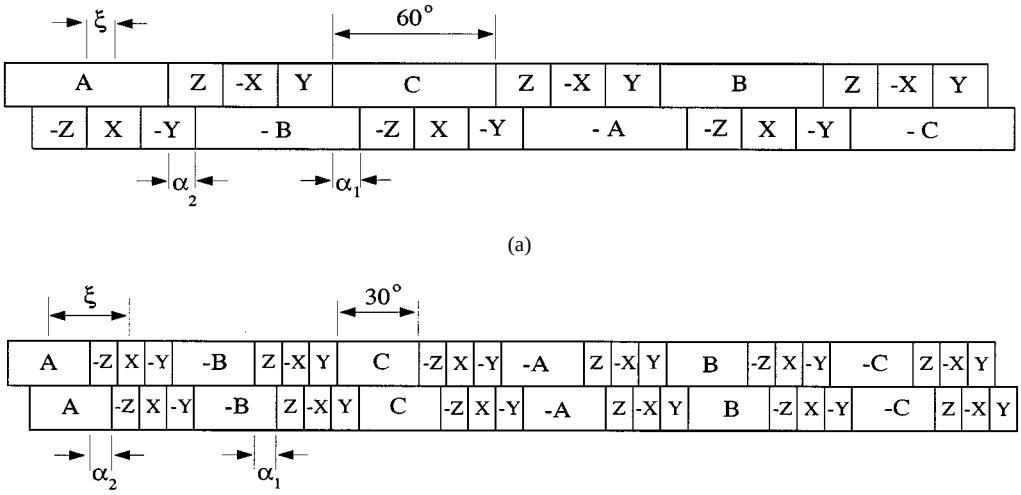

Fig. 6. Winding distribution for (a) fractional pitch and variable displacement angle ξ, $60°$ phase belt. (b) Fractional pitch and variable displacement angle ξ, $30°$ phase belt.

tance is $(3/2)L_{msi}$. The winding self-leakage inductance L_{lsi} is calculated by traditional methods [20], [21].

The submatrices $\boldsymbol{L}_{s12}$ and $\boldsymbol{L}_{s21}$ account for the mutual leakage coupling between the two stator windings. In general, the leakage flux can be divided into slot, end winding, belt, and zig-zag components, and each one of them will contribute to the self- and mutual leakage inductance. For simplicity, however, the mutual leakage due to the zig-zag and belt leakage components will be neglected and it will be assumed that they only contribute to the self-leakage. Therefore, it will be assumed that only the slot and end winding components contribute to the mutual leakage. Furthermore, it will be assumed that the end winding leakage varies as the slot leakage [19].

B. Slot Leakage Inductance

To study the mutual leakage term, let us consider the winding distributions shown in Fig. 6. They correspond to fractional pitch due to the displacement ξ between stators, $60°$ phase belt [Fig. 6(a)] and fractional pitch, $30°$ phase belt [Fig. 6(b)]. It should be noted that, because of the pole number, the pitch factors of each winding p_1 and p_2 are different. As shown by Alger [21] and Lipo [22], the slot leakage can be divided into self-leakage and mutual leakage. The self-leakage represents that part of the flux produced by the in-phase current component (i.e., slots with coil sides belonging to the same phase). The mutual leakage accounts for the leakage flux due to having conductors from different phases sharing common slots. In a two-layer winding the self L_{sls} and mutual L_{slm}, components of the slot leakage inductance can be expressed as a function of the pitch p as

$$L_{sls} = L_{lT} + L_{lB} + 2k_s(p)L_{lTB} \tag{6}$$

$$L_{slm} = k_m(p)L_{lTB} \tag{7}$$

where L_{lT} and L_{lB} are the slot leakage inductances associated to the coils in the top and bottom halves of the slots. They are calculated for the case of unity pitch and do not depend on winding pitch. The term L_{lTB} represents the mutual inductance between coils in the top and bottom halves of the slot. The quantities k_s and k_m are called slot factors and they correspond to proportionality constants that depend on the pitch.

For the winding distribution of Fig. 6(a), the phase belt slot leakage flux associated to phase a, when $8/9 < p_1 < 1$, is

$$\lambda_{sla} = (L_{lT1} + L_{lB1})i_{as} - L_{lTB1}k_{m1}(p_1)(i_{bs} + i_{cs}) + 2L_{lTB2}i_{xs} - (2 - k_{m2}(p_2))L_{lTB2}(i_{zs} + i_{ys}). \tag{8}$$

The equations applying to the remaining phases of the abc winding can be found by symmetry and the corresponding slot leakage matrix inductance is

$$\boldsymbol{L}_{sl1} = \begin{bmatrix} L_{lT1} + L_{lB1} & -L_{lTB1}k_{m1} & -L_{lTB1}k_{m1} \\ -L_{lTB1}k_{m1} & L_{lT1} + L_{lB1} & -L_{lTB1}k_{m1} \\ -L_{lTB1}k_{m1} & -L_{lTB1}k_{m1} & L_{lT1} + L_{lB1} \end{bmatrix} + 2L_{lTB2}\begin{bmatrix} 1 & k_{m2} - 2 & k_{m2} - 2 \\ 1 & k_{m2} - 2 & k_{m2} - 2 \\ 1 & k_{m2} - 2 & k_{m2} - 2 \end{bmatrix}. \tag{9}$$

Similarly, for the *xyz* winding,

$$\boldsymbol{L}_{sl2} = -L_{lTB2}\begin{bmatrix} -1 & -1 & -1 \\ 1 + k_{m2} & 1 + k_{m2} & 1 + k_{m2} \\ 1 + k_{m2} & 1 + k_{m2} & 1 + k_{m2} \end{bmatrix} + \begin{bmatrix} L_{lT2} + L_{lB2} & 0 & 0 \\ 0 & L_{lT2} + L_{lB2} & -3k_{m2}L_{lTB2} \\ 0 & -3k_{m2}L_{lTB2} & L_{lT2} + L_{lB2} \end{bmatrix}. \tag{10}$$

If the winding distribution of Fig. 6(b) is considered instead, the results are similar and the structure of (9) and (10) remain unchanged [16].

Assuming that the end-winding leakage behaves as the slot leakage, the mutual inductance matrix $\boldsymbol{L}_{s12}$ is proportional to the second term in (9). Clearly, the mutual inductance matrix $\boldsymbol{L}_{s21}$ will be proportional to the first term in (10).

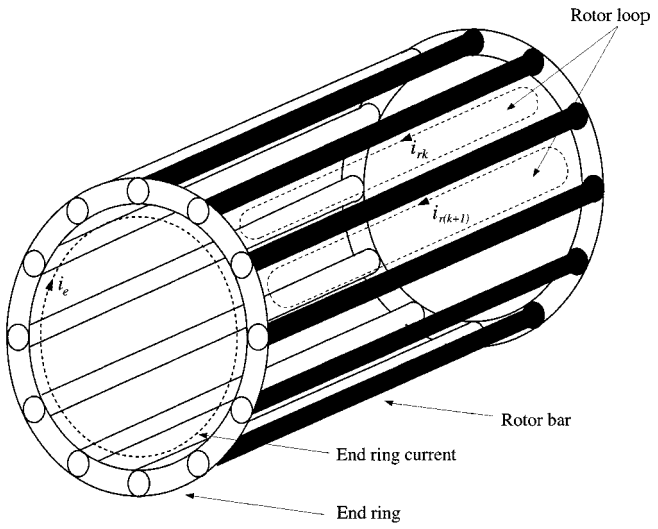

Fig. 7. Rotor current definition.

Given the symmetric structure of these matrices and assuming no neutral connection, it is apparent that after applying the space-vector definition

$$\underline{\boldsymbol{\lambda}}_{slabc} = \frac{2}{3}(\lambda_{sla} + \underline{a}\lambda_{slb} + \underline{a}^2\lambda_{slc}) \tag{11}$$

their contribution to the total flux vector will be zero.

This result is very important since it proves that both stator windings are fully decoupled and the total flux linked by the stator windings can be written as

$$\boldsymbol{\Lambda}_{sabc} = \boldsymbol{L}_{s1}\boldsymbol{i}_{sabc} + \boldsymbol{L}_{sr1}\boldsymbol{i}_r \tag{12}$$

for the abc winding and

$$\boldsymbol{\Lambda}_{sxyz} = \boldsymbol{L}_{s2}\boldsymbol{i}_{sxyz} + \boldsymbol{L}_{sr2}\boldsymbol{i}_r \tag{13}$$

for the *xyz* winding. The matrices $\boldsymbol{L}_{sr1}$ and $\boldsymbol{L}_{sr2}$ describe the mutual coupling between the stator and rotor circuits and they can be found using winding functions [23]. The resultant stator flux associated with the *abc* winding is given by [23]

$$\underline{\boldsymbol{\lambda}}_{sabc} = \left(L_{ls1} + \frac{3}{2}L_{ms1}\right)\underline{\boldsymbol{i}}_{s1} + \frac{2n\sin\delta}{\pi N_{s1}}L_{ms1}\,e^{j(\theta_r+\delta)}\underline{\boldsymbol{i}}_{r1} \tag{14}$$

where n is the number of rotor bars, 2δ is the angle between rotor bars, and the complex vector currents $\underline{\boldsymbol{i}}_{s1}$ and $\underline{\boldsymbol{i}}_{r1}$ are defined by

$$\underline{\boldsymbol{i}}_{s1} = \frac{2}{3}(i_{as} + \underline{a}i_{bs} + \underline{a}^2 i_{cs}) \tag{15}$$

$$\underline{\boldsymbol{i}}_{r1} = \frac{2}{n}\begin{bmatrix}1 & \underline{b} & \underline{b}^2 & \cdots & \underline{b}^{n-1}\end{bmatrix}\begin{bmatrix}i_{r1}\\ i_{r2}\\ \vdots\\ i_{rn}\end{bmatrix} \tag{16}$$

with $\underline{a} = e^{j2\pi/3}$ and $\underline{b} = e^{j2\pi/n}$. The vector $[i_{r1}\ \ i_{r2}\ \cdots\ i_{rn}]^T$ represents the instantaneous rotor currents defined according to Fig. 7.

A similar analysis for the xyz winding yields [16]

$$\underline{\boldsymbol{\lambda}}_{sxyz} = \left(L_{ls2} + \tfrac{3}{2}L_{ms2}\right)\underline{\boldsymbol{i}}_{s2} + \frac{2n\sin\dfrac{P}{2}\delta}{\pi N_{s2}}L_{ms2}\,e^{j(P/2)(\theta_r+\delta-\xi)}\underline{\boldsymbol{i}}_{r2} \tag{17}$$

where

$$\underline{\boldsymbol{i}}_{s2} = \frac{2}{3}(i_{xs} + \underline{a}i_{ys} + \underline{a}^2 i_{zs}) \tag{18}$$

and

$$\underline{\boldsymbol{i}}_{r2} = \frac{2}{n}\begin{bmatrix}1 & \underline{b}^{P/2} & \underline{b}^{(P/2)2} & \cdots & \underline{b}^{(P/2)(n-1)}\end{bmatrix}\begin{bmatrix}i_{r1}\\ i_{r2}\\ \vdots\\ i_{rn}\end{bmatrix}. \tag{19}$$

Note that, because of the different number of poles considered in this case, it is necessary to define a new rotor current space vector $\underline{\boldsymbol{i}}_{r2}$. The physical meaning of this new definition can be understood by recognizing that the equivalent electrical angle between adjacent rotor bars, referred to the P-pole winding, is now $(P/2)\theta_r$ instead of θ_r. Also note that the instantaneous rotor bar currents in (16) and (19) are the same.

Finally, the two stator voltage equations are obtained by differentiating the flux linkages (14) and (17) and adding the resistive voltage drops, yielding

$$\underline{\boldsymbol{v}}_{s1} = r_{s1}\underline{\boldsymbol{i}}_{s1} + \left(L_{ls1} + \frac{3}{2}L_{ms1}\right)p\underline{\boldsymbol{i}}_{s1} + \frac{2n\sin\delta}{\pi N_{s1}}L_{ms1}\,e^{j(\theta_r+\delta)}(p + j\omega_r)\underline{\boldsymbol{i}}_{r1} \tag{20}$$

for the abc winding and

$$\underline{\boldsymbol{v}}_{s2} = r_{s2}\underline{\boldsymbol{i}}_{s2} + \left(L_{ls2} + \frac{3}{2}L_{ms2}\right)p\underline{\boldsymbol{i}}_{s2} + \frac{2n\sin\dfrac{P}{2}\delta}{\pi N_{s2}}L_{ms2}e^{j(P/2)(\theta_r+\delta-\xi)}\left(p + j\frac{P}{2}\omega_r\right)\underline{\boldsymbol{i}}_{r2} \tag{21}$$

for the xyz winding, with $\underline{\boldsymbol{v}}_{s1}$ and $\underline{\boldsymbol{v}}_{s2}$ given by

$$\underline{\boldsymbol{v}}_{s1} = \frac{2}{3}(v_{as} + \underline{a}v_{bs} + \underline{a}^2 v_{cs})$$
$$\underline{\boldsymbol{v}}_{s2} = \frac{2}{3}(v_{xs} + \underline{a}v_{ys} + \underline{a}^2 v_{zs}). \tag{22}$$

It is important to notice that the stator current $\underline{\boldsymbol{i}}_{s1}$ depends only on the applied voltage $\underline{\boldsymbol{v}}_{s1}$ and the rotor current $\underline{\boldsymbol{i}}_{r1}$. Similarly, the current $\underline{\boldsymbol{i}}_{s2}$ depends only on the applied voltage $\underline{\boldsymbol{v}}_{s2}$ and the rotor current $\underline{\boldsymbol{i}}_{r2}$. This result verifies the known fact that, for a sinusoidally distributed winding, there only exists coupling between current distributions of the same number of poles. It should also be pointed out that, for a distributed winding, the number of turns used in the foregoing equations corresponds to the effective number of turns (i.e., they include the winding factors).

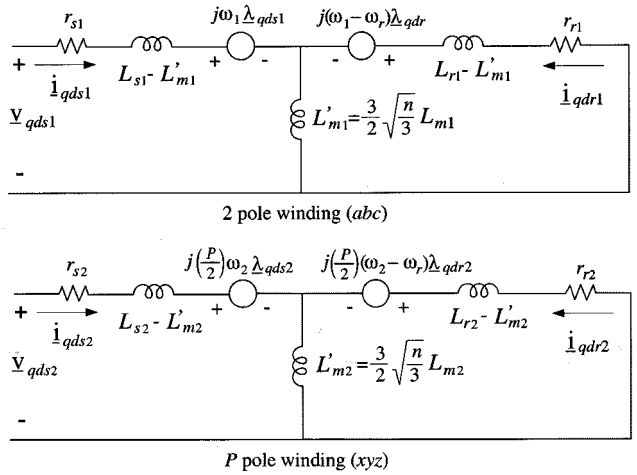

Fig. 8. Complex vector model of the dual stator winding squirrel-cage induction machine.

C. Rotor Flux

The rotor flux can be divided into three components, one due to the rotor currents $\boldsymbol{i}_r$ and two due to the stator currents $\boldsymbol{i}_{sabc}$ and $\boldsymbol{i}_{sxyz}$. In matrix form,

$$\begin{bmatrix} \lambda_{r1} \\ \lambda_{r2} \\ \vdots \\ \lambda_{rn} \end{bmatrix} = \boldsymbol{L}_r \begin{bmatrix} i_{r1} \\ i_{r2} \\ \vdots \\ i_{rn} \end{bmatrix} + \boldsymbol{L}_{rs1} \begin{bmatrix} i_{as} \\ i_{bs} \\ i_{cs} \end{bmatrix} + \boldsymbol{L}_{rs2} \begin{bmatrix} i_{xs} \\ i_{ys} \\ i_{zs} \end{bmatrix}. \quad (23)$$

The complex vector representation of the rotor flux is defined by the vector transformation

$$\underline{\boldsymbol{\lambda}}_r = \frac{2}{n} \begin{bmatrix} 1 & \underline{b}^{P/2} & \underline{b}^{(P/2)2} & \cdots & \underline{b}^{(P/2)(n-1)} \end{bmatrix} \begin{bmatrix} \lambda_{r1} \\ \lambda_{r2} \\ \vdots \\ \lambda_{rn} \end{bmatrix} \quad (24)$$

where P is given by the number of poles of the stator winding. Setting $P = 2$ in (24) and applying it to (25) yields the rotor flux referred to the abc winding.

It is clear that the first two terms of (23) correspond to those of a single stator machine, thus [23]

$$\underline{\boldsymbol{\lambda}}_{rr} = \underbrace{\left(2L_b(1-\cos\alpha_r) + 2L_e + \frac{\mu_o l r}{g}\alpha_r\right)}_{L_{r1}} \underline{\boldsymbol{i}}_{r1} \quad (25)$$

and

$$\underline{\boldsymbol{\lambda}}_{rs1} = \frac{6\sin\delta}{\pi N_{s1}} L_{ms1}\, e^{-j(\theta_r+\delta)} \underline{\boldsymbol{i}}_{s1} \quad (26)$$

where L_b and L_e represent the bar and end-ring segment inductance respectively and g is the air-gap length.

The last term of (23) represents the contribution due to the xyz currents. Following the same technique, it can be shown that

$$\underline{\boldsymbol{\lambda}}_{rs2} = \frac{2\sin\frac{P}{2}\delta}{\pi N_{s2}} L_{ms2} \left\{ e^{j(P/2)(\theta_r+\delta-\xi)} \underline{\boldsymbol{i}}^*_{s2} \sum_{i=0}^{n-1} \underline{b}^{((P/2)+1)i} + e^{-j(P/2)(\theta_r+\delta-\xi)} \underline{\boldsymbol{i}}_{s2} \sum_{i=0}^{n-1} \underline{b}^{-((P/2)-1)i} \right\}. \quad (27)$$

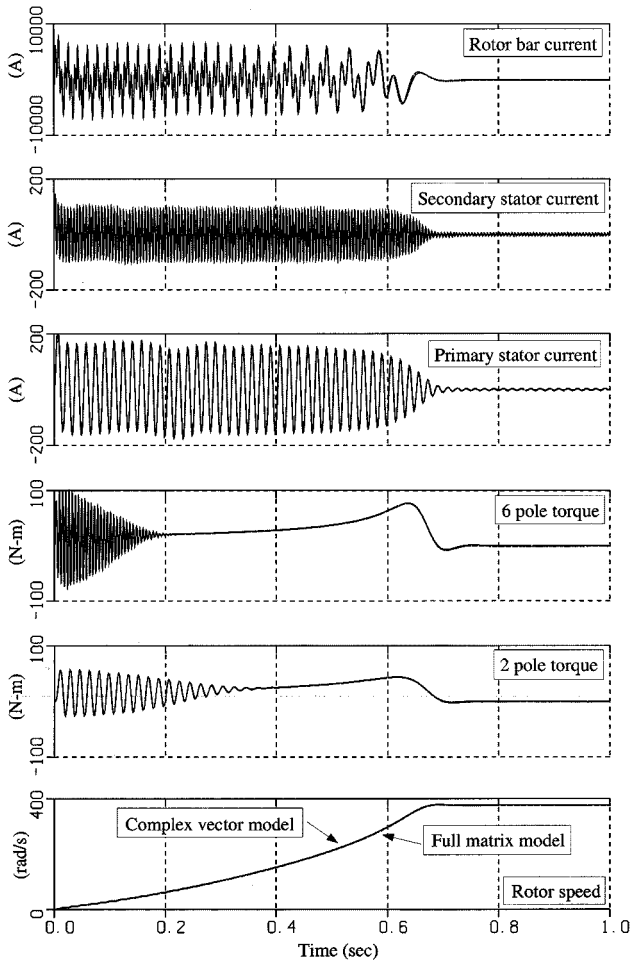

Fig. 9. Full matrix and complex vector model simulation results for a free acceleration run at 60 Hz ($f_2 = 180$ Hz). Complex vector and full matrix model traces are superimposed.

Evaluating (27) for $P > 2$ results in both summations being identically zero regardless of the value of $\underline{\boldsymbol{i}}_{s2}$, hence, the total rotor flux, in the $\underline{\boldsymbol{i}}_{r1}$ subspace, corresponds to the sum of (25) and (26).

Finally, taking the time derivative of the rotor flux vector and adding the resistive voltage drop yields the rotor voltage equation in the subspace defined by $\underline{\boldsymbol{i}}_{r1}$

$$\underline{\boldsymbol{0}} = r_{r1}\underline{\boldsymbol{i}}_{r1} + L_{r1}p\underline{\boldsymbol{i}}_{r1} + \frac{6\sin\delta}{\pi N_{s1}} L_{ms1}\, e^{-j(\theta_r+\delta)}(p - j\omega_r)\underline{\boldsymbol{i}}_{s1} \quad (28)$$

with $r_{r1} = 2R_e + 2R_b(1-\cos\alpha_r)$.

A similar analysis for the P-pole winding reveals that, in this case, the contribution of the second term in (23) is zero, hence, the rotor equation in the subspace defined by $\underline{\boldsymbol{i}}_{r2}$ is

$$\underline{\boldsymbol{0}} = r_{r2}\underline{\boldsymbol{i}}_{r2} + L_{r2}p\underline{\boldsymbol{i}}_{r2} + \frac{6\sin\frac{P}{2}\delta}{\pi N_{s2}} L_{ms2} \cdot e^{-j(P/2)(\theta_r+\delta-\xi)} \left(p - j\frac{P}{2}\omega_r\right)\underline{\boldsymbol{i}}_{s2} \quad (29)$$

where r_{r2} represents the equivalent rotor resistance and L_{r2} is the equivalent rotor inductance in the new subspace

$$r_{r2} = 2R_e + 2R_b\left[1 - \cos\left(\frac{P}{2}\alpha_r\right)\right] \quad (30)$$

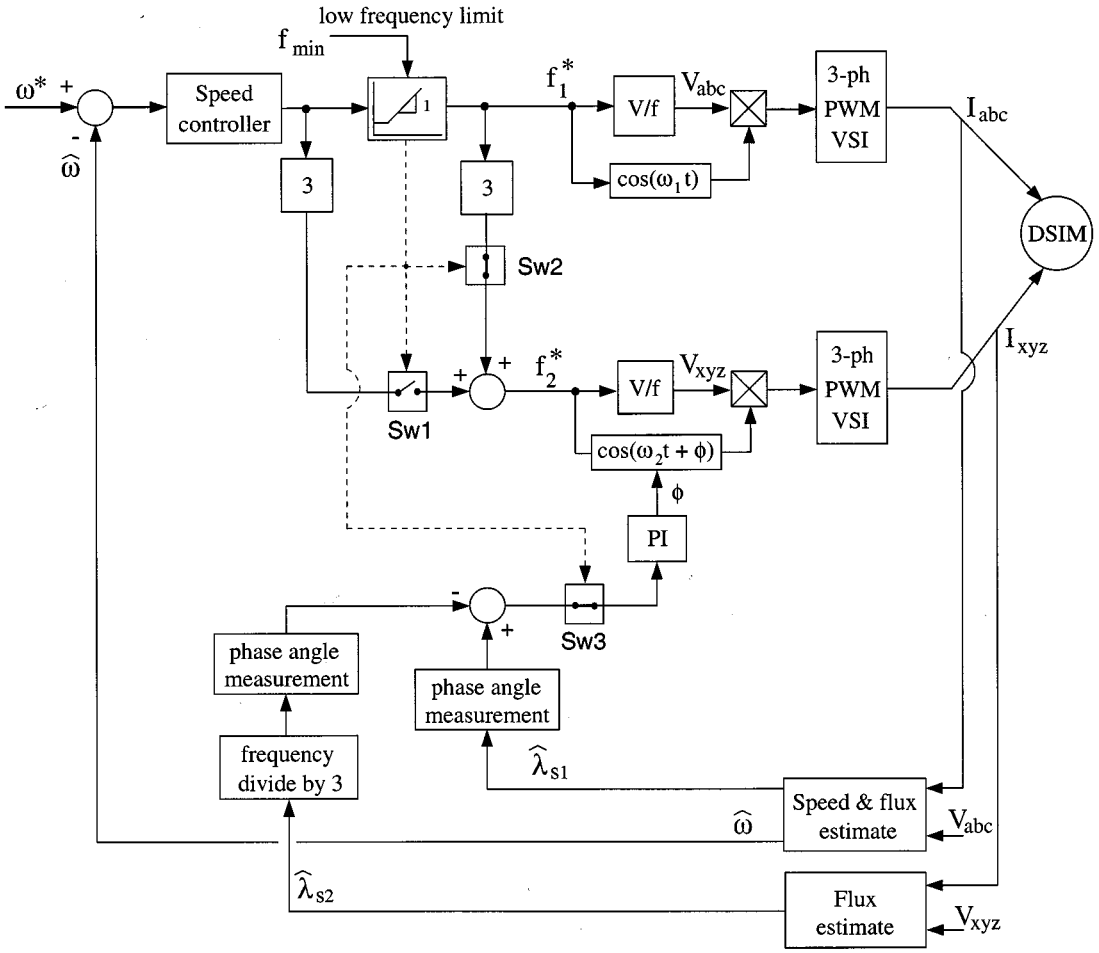

Fig. 10. Proposed control scheme using constant volts per hertz (V/Hz) mode.

and

$$L_{r2} = 2L_b\left[1-\cos\left(\frac{P}{2}\,\alpha_r\right)\right] + 2L_e + \frac{\mu_o l r}{g}\left(\frac{P}{2}\,\alpha_r\right). \tag{31}$$

Note that although the instantaneous rotor current distribution contains two frequency components, each stator field is capable of interacting only with that part of the rotor field with the "correct" number of poles. This is true not only in an average basis, but also instantaneously. It is well known that sinusoidally distributed windings only couple with fields of equal number of poles, however, the rotor cage is clearly not a sinusoidal winding and one might expect that the presence of two superimposed flux distributions would give rise to pulsating torques. However, this is not the case for the DSIM. An equivalent circuit, using d–q notation, is shown in Fig. 8.

Neglecting saturation, the electromagnetic torque can be expressed as the partial variation of the co-energy with respect to position [17]

$$T_e = \left[\boldsymbol{i}_{sabc}^T \;\; \boldsymbol{i}_{sxyz}^T\right] \frac{\partial}{\partial \theta_r}\begin{bmatrix}\boldsymbol{L}_{sr1}\\ \boldsymbol{L}_{sr2}\end{bmatrix} \boldsymbol{i}_r. \tag{32}$$

Substituting the corresponding matrices and carrying out the differentiation yields

$$T_e = -\left(\frac{3n\,\sin\delta}{\pi N_{s1}}\right) L_{ms1} \cdot \mathrm{Im}\left\{ e^{j(\theta_r+\delta)}\,\underline{\boldsymbol{i}}_{s1}^{*}\,\underline{\boldsymbol{i}}_{r1} + e^{j(P/2)(\theta_r+\delta-\xi)} \cdot \frac{2N_{s2}\,\sin\left(\frac{P}{2}\delta\right)}{PN_{s1}\,\sin\delta}\,\underline{\boldsymbol{i}}_{s2}^{*}\,\underline{\boldsymbol{i}}_{r2}\right\}. \tag{33}$$

Since $\underline{\boldsymbol{i}}_{r1}$ and $\underline{\boldsymbol{i}}_{r2}$ are orthogonal vectors, each torque component can be controlled independently. This is a key feature of the proposed drive. To validate the complex space-vector model of the DSIM, a complete set of simulations was carried out. The results from the space-vector model were compared to those obtained from a full matrix model of the machine. Fig. 9 shows both set of results superimposed. Clearly, both simulations are identical, thus validating the complex vector model developed. As shown in Fig. 9, the rotor currents contain two frequencies dictated by the frequency of each of the stator currents and the

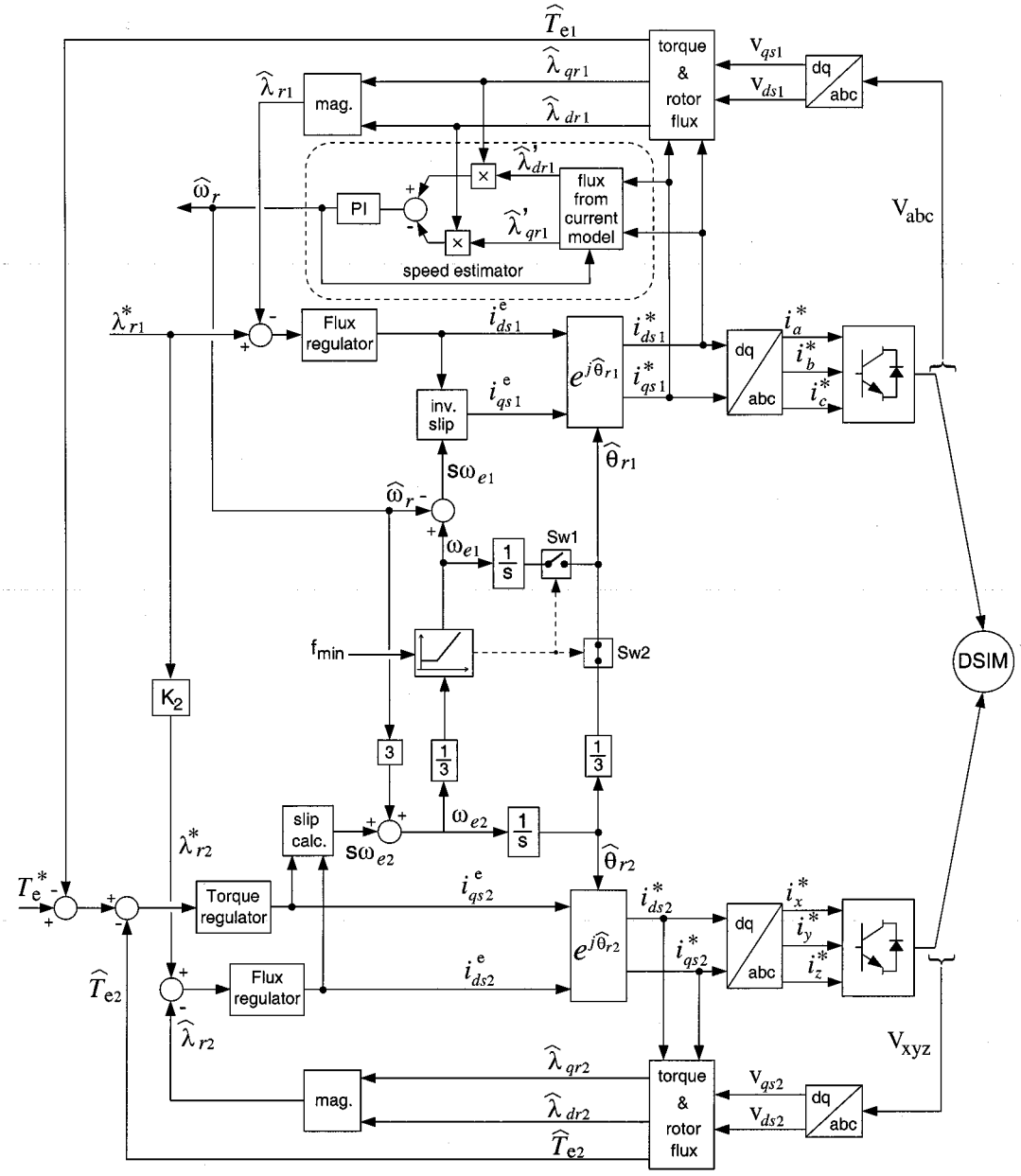

Fig. 11. Proposed control scheme using indirect field orientation.

rotor mechanical speed. Although the rotor currents simultaneously produce two field distributions that rotate at different speeds, because of the different number of poles and the sinusoidal characteristic of the stator windings, they do not give rise to harmonic torques.

IV. Torque and Speed Control

The DSIM behaves as two independent induction machines, mechanically coupled through the shaft. Therefore, all known control techniques used in induction motor drives are also applicable to the DSIM. However, because of the common magnetic structure some additional consideration must be given to maintain the correct flux level.

Two distinct operating modes are defined: *synchronous* operation where the stator frequencies are in the same ratio as the pole number and *asynchronous* operation where the frequency in the low-pole number winding is kept constant at a minimum value (≈2.5 Hz), regardless of the mechanical speed. This mode is used to achieve zero-speed operation. In this case, the two stator MMFs move asynchronously and the resultant flux distribution is distorted, causing localized saturation. However, because of the low frequency, the additional losses are negligible. During *synchronous* operation, both MMFs move synchronously and the resultant air-gap flux distribution corresponds to that shown in Fig. 3. The goal of the control technique is to always maintain the stator frequency at or above a minimum value, regardless of the mechanical speed. This enables

the use of simple straightforward speed/flux estimation algorithms for sensorless operation.

A. Constant V/Hz

The operation and control will be explained using Fig. 4. As shown, there are two operating modes. For high speed, both stators are fed with voltages of the same frequency (i.e., *synchronous* mode). This produces the torque–speed curves of Fig. 4(a), which have been exaggerated for clarity. The output torque for a given rotor speed corresponds to the algebraic sum of the torques T_1 and T_2. The torque produced by each winding is controlled by adjusting the magnitude of the stator voltages.

When the mechanical speed demands a frequency below the minimum value, the frequency of the abc winding is fixed and the output torque is adjusted by controlling the frequency (and voltage) supplied to the xyz winding. This corresponds to the *asynchronous* mode and is shown in Fig. 4(b). In this case, one of the stator windings (abc) operates in the motoring region while the other (xyz) operates as a generator. Note that this operating mode corresponds to the one required to operate at zero speed and that the torque can be controlled from zero to rated value. A block diagram of the proposed control scheme is shown in Fig. 10. To maintain the correct magnetic loading in the *synchronous* mode, the relative phase angle of the xyz voltages is adjusted by the feedback loop shown. During *asynchronous* operation, this loop is deactivated.

B. Vector Control

The proposed control scheme is shown in Fig. 11. There are two operating modes: a high speed range defined by frequencies above a minimum frequency $f_{\min}$ (*synchronous* mode) and a low speed range for frequencies below (*asynchronous* mode). In the *synchronous* mode, a standard indirect field orientation based on the slip relation is used. The estimated torque produced by the abc currents, $\hat{T}_{e1}$, is subtracted off the external torque command T_e^* to produce the torque command for the xyz winding T_{e2}^*. The slip frequency $s\omega_{e2}$ is computed using the commanded flux producing, i_{ds2}^e, and torque producing, i_{qs2}^e, current components. To maintain the correct flux orientation of the low-pole number winding, the commanded torque producing current i_{qs1}^e is computed using the inverse of the slip relation.

For low-speed operation (i.e., *asynchronous* mode) the commanded frequency ω_{e1} is clamped at $\omega_{\min} = 2\pi f_{\min}$. This frequency, together with the rotor speed, defines the slip frequency used to compute the torque-producing current i_{qs1}^e. To maintain the orientation of the rotor flux, the vector rotation angle θ_{r1} is computed as the integral of the input frequency ω_{e1}. Since this operating mode forces the low-pole winding to produce a torque in excess of that of the load, the extra torque is compensated by an equal and opposite torque produced by the high-pole number winding.

V. Simulation Results

Simulation results using the control techniques proposed in the previous section are shown in Figs. 12 and 13. The results prove the feasibility of the concept and clearly show the operation at zero speed and no-load while keeping the stator frequency at or above the minimum frequency.

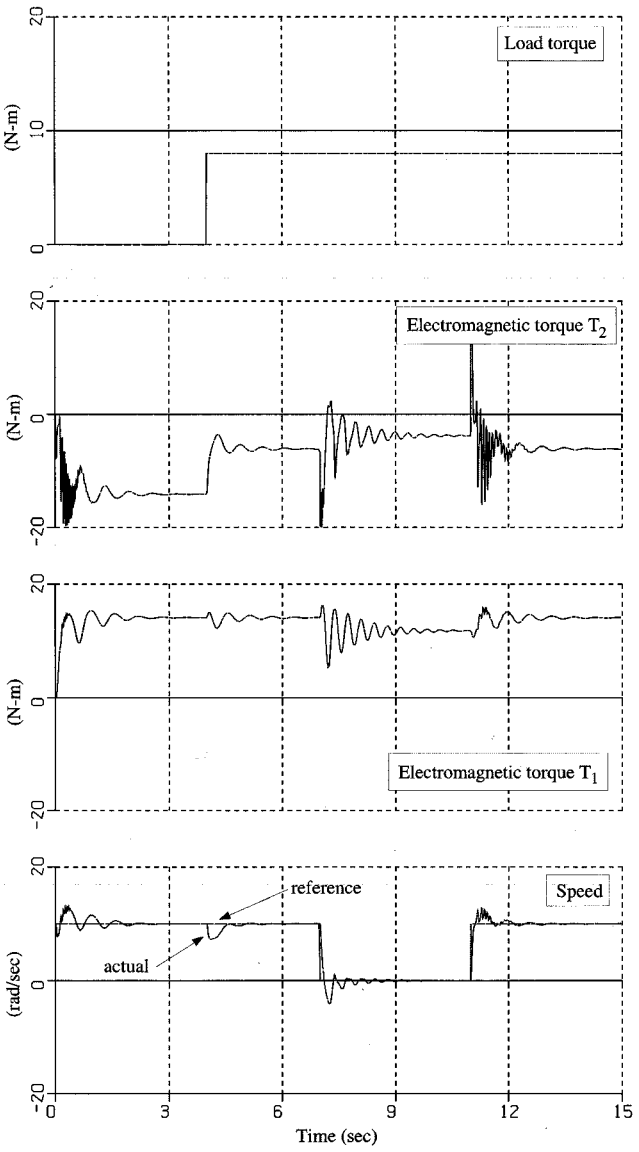

Fig. 12. Constant V/Hz operation at standstill.

VI. Experimental Results

The experimental work was carried out using a 3-kW prototype wound for a 4/12-pole combination. A six-leg inverter with a 300-V dc bus was used. The control software was implemented in a Motorola 56000 DSP and the rotor position was estimated by integrating the terminal voltages. Zero-speed operation using constant V/Hz and indirect field orientation are shown in Figs. 14 and 15. The response in both cases is excellent, showing a very stable and accurate operation.

VII. Conclusions

A new type of dual stator winding induction machine has been presented. The proposed DSIM has a standard squirrel-cage rotor

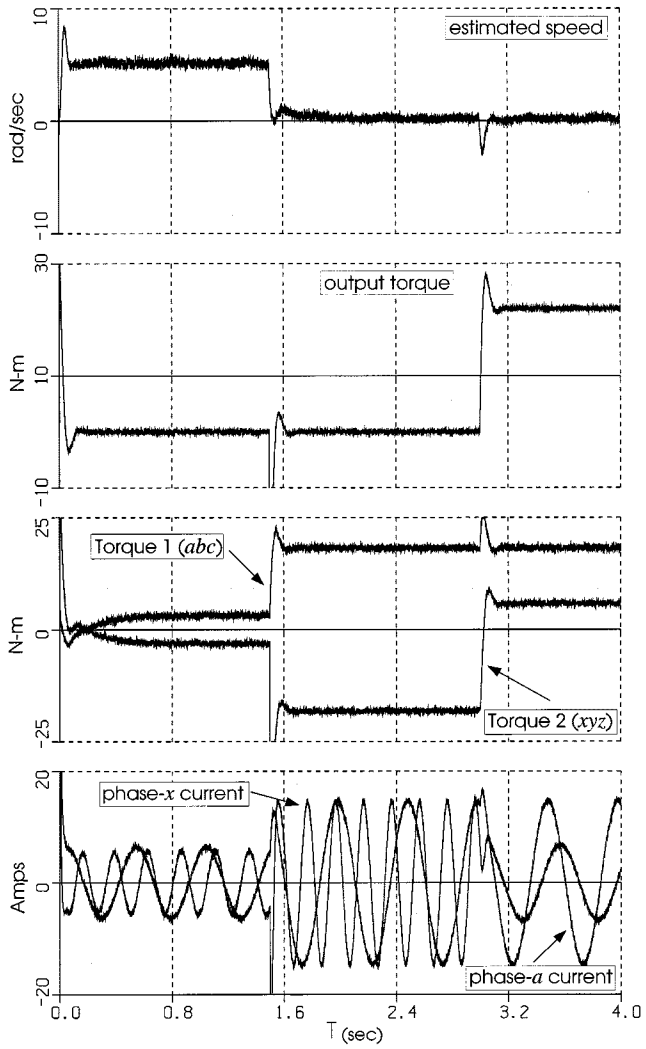

Fig. 13. Direct field orientation during *asynchronous* operation.

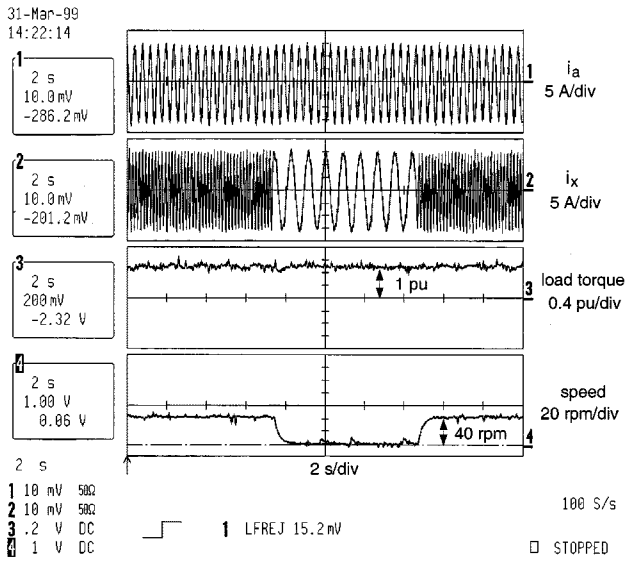

Fig. 14. Constant V/Hz operation in *asynchronous* mode. From top: phase-a current, phase-x current, load torque, and speed.

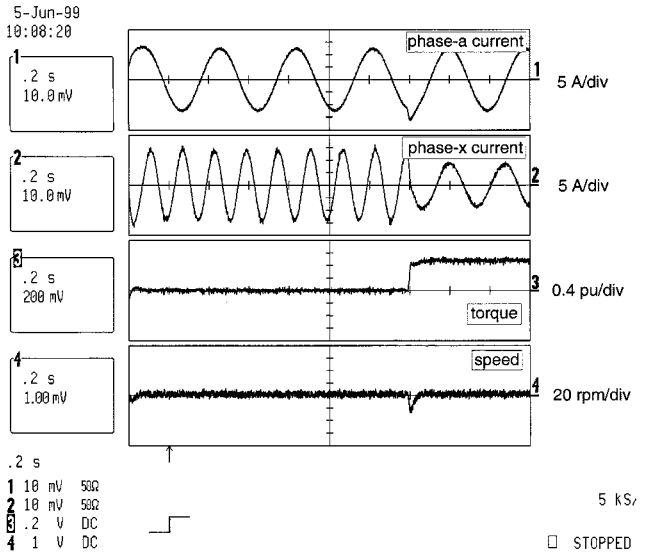

Fig. 15. Indirect field orientation in *asynchronous* mode. From top: phase-a current, phase-x current, load torque, and speed.

and two stator windings wound for a dissimilar number of poles. The main advantage of the drive is its improved capability to operate at low and zero speeds, maintaining relatively high stator frequencies. This feature is particularly useful for implementation of speed sensorless schemes and it adds a new degree of flexibility to standard control methods currently used in ac drives. Two control schemes have been proposed, simulated, and tested using a prototype, showing very good performance. The DSIM is especially well suited for both scalar constant V/Hz and vector control.

A detailed design of the DSIM and performance comparison with a standard induction machine is reported in a separate paper, which is to be published.

REFERENCES

[1] P. L. Alger, E. H. Freiburghouse, and D. D. Chase, "Double windings for turbine alternators," *AIEE Trans.*, vol. 49, pp. 226–244, Jan. 1930.

[2] P. W. Franklin, "A theoretical study of the three phase salient pole type generator with simultaneous AC and bridge rectified DC output," *IEEE Trans. Power App. Syst.*, vol. PAS-92, no. 2, pp. 543–557, Mar./Apr. 1973.

[3] R. Schiferl, "Detailed analysis of a six phase synchronous machine with AC and DC stator connections," Ph.D. dissertation, Elect. Eng. Dep., Purdue Univ., West Lafayette, IN, 1982.

[4] T. Kataoka, E. H. Watanabe, and J. Kitano, "Dynamic control of a current-source inverter/double-wound synchronous machine system for AC power supply," *IEEE Trans. Ind. Applicat.*, vol. IA-17, pp. 314–320, May/June 1981.

[5] R. W. Menzies, P. Steimer, and J. K. Steinke, "Five-level GTO inverters for large induction motor drives," *IEEE Trans. Ind. Applicat.*, vol. 30, pp. 938–944, July/Aug. 1994.

[6] T. M. Jahns, "Improved reliability in solid state AC drives by means of multiple independent phase drive units," *IEEE Trans. Ind. Applicat.*, vol. IA-16, pp. 321–331, May/June 1980.

[7] J. R. Fu and T. A. Lipo, "Disturbance free operation of a multiphase current regulated motor drive with an opened phase," *IEEE Trans. Industry Applicat.*, vol. 30, pp. 1267–1274, Sept./Oct. 1994.

[8] J. C. Salmon and B. W. Williams, "A split-wound induction motor design to improve the reliability of PWM inverter drives," *IEEE Trans. Ind. Applicat.*, vol. IA-26, pp. 143–150, Jan./Feb. 1990.

[9] K. Gopakumar, V. T. Ranganathan, and S. R. Bhat, "Split-phase induction motor operation from PWM voltage source inverter," *IEEE Trans. Ind. Applicat.*, vol. 29, pp. 927–932, Sept./Oct. 1993.
[10] L. J. Hunt, "A new type of induction motor," *J. Inst. Elect. Eng.*, vol. 39, pp. 648–677, 1907.
[11] A. R. Broadway and L. Burbridge, "Self-cascaded machine: A low-speed motor or high frequency brushless alternator," *Proc. Inst. Elect. Eng.*, vol. 117, pp. 1277–1290, July 1970.
[12] B. Koch, R. Spée, and B. Clever, "A comparison of stack preparation methods for bar insulation in diecast rotors," in *Conf. Rec. IEEE-IAS Annu. Meeting*, New Orleans, LA, Oct. 1997, pp. 182–187.
[13] S. Williamson and M. Boger, "Impact of inter-bar currents on the performance of the brushless doubly-fed motor," in *Conf. Rec. IEEE-IAS Annu. Meeting*, New Orleans, LA, Oct. 1997, pp. 188–195.
[14] A. K. Wallace, R. Spée, and H. K. Lauw, "Dynamic modeling of brushless doubly-fed machines," in *Conf. Rec. IEEE-IAS Annu. Meeting*, San Diego, CA, Oct. 1989, pp. 329–334.
[15] P. Rochelle, R. Spée, and A. Wallace, "The effect of stator winding configuration on the performance of brushless doubly-fed machines in adjustable speed drives," in *Conf. Rec. IEEE-IAS Annu. Meeting*, Seattle, WA, Oct. 1990, pp. 331–337.
[16] A. R. Muñoz-García, "Analysis and control of a dual stator winding squirrel cage induction machine," Ph.D. dissertation, Dep. Elect. Comput. Eng., Univ. Wisconsin, Madison, 1999.
[17] D. W. Novotny and T. A. Lipo, *Vector Control and Dynamics of AC Drives*. Oxford, U.K.: Clarendon, 1996.
[18] S. A. Nasar, "Electromechanical energy conversion in nm-winding double cylindrical structures in presence of space harmonics," *IEEE Trans. Power App. Syst.*, vol. PAS-87, pp. 1099–1106, Apr. 1968.
[19] T. A. Lipo, "A d–q model for six phase induction machines," in *Proc. Int. Conf. Electric Machines*, Athens, Greece, 1980, pp. 860–867.
[20] A. S. Langsdorf, *Theory of Alternating Current Machinery*, 2nd ed. New York: McGraw-Hill, 1955.
[21] P. L. Alger, *Induction Machines*, 2nd ed. New York: Gordon and Breach, 1970.
[22] T. A. Lipo, *Introduction to AC Machine Design*. Madison, WI: Univ. of Wisconsin Press, 1996.
[23] A. R. Muñoz and T. A. Lipo, "Complex vector model of the squirrel cage induction machine including instantaneous rotor bar currents," *IEEE Trans. Ind. Applicat.*, vol. 35, pp. 1332–1340, Nov./Dec. 1999.

Alfredo R. Muñoz (M'87) was born in Valparaíso, Chile. He received the B.S. degree from the Technical University Santa María, Valparaíso, Chile, and the M.S. and Ph.D. degrees from the University of Wisconsin, Madison, in 1981, 1995, and 1999 respectively, all in electrical engineering.

From 1981 to 1986, he was with Schlumberger Overseas. In 1987, he became a full-time Lecturer and, in 1989, an Assistant Professor in the Electrical Engineering Department, Technical University Santa María. He was a Fulbright Fellow from 1993 to 1995. From 1993 to 1999, he was a Research Assistant at the University of Wisconsin, Madison. He recently joined the Scientific Research Laboratory, Ford Motor Company, Dearborn, MI. His main research interests include electric machines, ac drives, and power electronics. He has authored several published papers on variable-frequency drives and power electronics,

Dr. Muñoz was the recipient of the Third Prize Paper Award from the Electric Machines Committee at the 1998 IEEE Industry Applications Society Annual Meeting.

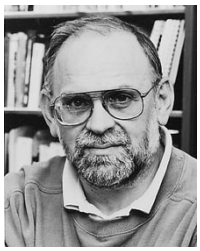

Thomas A. Lipo (M'64–SM'71–F'87) is a native of Milwaukee, WI. From 1969 to 1979, he was an Electrical Engineer in the Power Electronics Laboratory, Corporate Research and Development, General Electric Company, Schenectady NY. He became a Professor of electrical engineering at Purdue University, West Lafayette, IN, in 1979 and, in 1981, he joined the University of Wisconsin, Madison, in the same capacity, where he is presently the W. W. Grainger Professor for power electronics and electrical machines.

Dr. Lipo has received the Outstanding Achievement Award from the IEEE Industry Applications Society, the William E. Newell Award of the IEEE Power Electronics Society, and the 1995 Nicola Tesla IEEE Field Award from the IEEE Power Engineering Society for his work. Over the past 30 years, he has served the IEEE in numerous capacities, including President of the IEEE Industry Applications Society.